WILEY | Hindawi

Research Article

Influence of the Preexisting Fracture Network on the Mechanical Properties of Rock Mass and the Secondary Crack Propagation

Ping Guo [iD],[1] **Guodong Li** [iD],[2,3] **Feng Luo**,[2,3] **and Xiaojun Tang**[1]

[1]*School of Architectural Engineering, Chongqing Industry Polytechnic College, Chongqing, China*
[2]*School of Mining and Geomatics Engineering, Hebei University of Engineering, Handan, China*
[3]*Hebei Coal Mine Construction Engineering Technology Research Center, Handan, China*

Correspondence should be addressed to Guodong Li; gd.li@cqu.edu.cn

Preexisting fracture network (PFN) is ubiquitous in natural rock mass and is one of the key factors affecting the mechanical properties of rock mass. This research employed a combined approach of theoretical analysis and finite element numerical simulation to investigate the mechanical behavior of PFN-containing rock mass. Based on the sliding crack model and fracture mechanics theory, the initiation mechanism of closed and open cracks driven by compressive and shear stress was theoretically analyzed. Rock mass models with different inclination angles (β) of PFN were built in Fast Lagrangian Analysis of Continua in 3 Dimensions. The complete stress–strain curves of rock mass and the secondary crack propagation were obtained. Results indicated that the increase of β reduced the strength and elastic modulus of rock mass. When β is less than 45°, this influence is more prominent. Based on the load-bearing capacity of PFN-containing rock mass, the stress–strain curves can be classified into two types: type I curve has multipeak and is strain-softening in the postpeak stage when β is 15°, 30°, 45°, 60°, and 90°; type II curve is unimodal and with brittle failure when β is 60° and 75°. Secondary crack propagation can be classified into four main types: type I is the coplanar crack, type II is the wing crack around PFN, type III is the near-field wing crack, and type IV is the macroscopic shear crack.

1. Introduction

Due to the active tectonic movement in history, many fractures and cracks have been generated inside engineering rock mass, and the fractures usually occur in groups in nature (Figure 1). It is also known as preexisting fracture network (PFN) or joint set. Blasting and excavation in rock engineering may cause secondary crack initiation, propagation, and coalescence. The secondary crack developed from PFN degrades the mechanical properties of rock mass and weakens the relative sliding of coplanar fractures. It also affects secondary crack coalescence and rock mass macrofailure. The load-bearing ability of rock mass is the base of supporting and mining design, and unexpected fracture development is a potential threat to the safety of rock engineering projects. Therefore, studying PFN development and obtaining the mechanical prosperities of PFN-containing rock mass are the prerequisites for the stability analysis and support design of rock mass [1, 2].

The newly emerged crack in a rock mass can be called a secondary crack, which is developed from a primary fracture under compaction. Secondary crack propagation is listed as one of the most fundamental issues in experimental and theoretical research in rock mechanics. Griffith studied the growth of the preexisting 2D crack in 1924 [3]. Based on the energy release rate and stress concentration during the crack extension, Irwin introduced the adjustable uniform stress and stress-intensity factor to quantitatively investigate crack initiation conditions [4]. Then, many scholars researched about secondary crack classification, the macroscopic mechanical behavior of fractured rock mass, and the mechanical model of crack propagation [5–7]. The location and extension mode and the special relationship with the primary crack are often used to classify the secondary crack [8, 9].
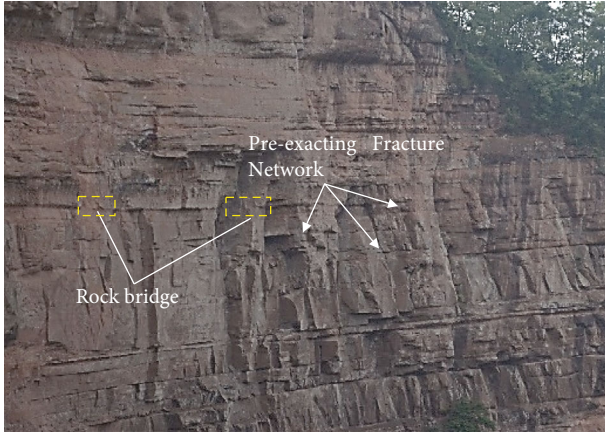
FIGURE 1: PFN-containing rock mass.

FIGURE 2: The secondary crack propagation.

The change in the inclination angle of PFN leads to an increase in the heterogeneity of rock mass and affects the distribution of the internal stress field [10]. The geometry of PFN, including the number, size, opening, dip angle of the fracture, and the width of rock bridge, is the critical factor that affects the mechanical properties of PFN-containing rock mass and the secondary crack propagation [11, 12]. Preparing samples with natural PFN in the laboratory is difficult, so rock-like materials, such as gypsum, mortar, and resin, are used to make specimens to represent rock, and PFN can be introduced into the specimen by cutting or prefabricating [13]. Digital photography and image processing technologies are selected to observe surface crack details. The Acoustic Emission source location, Computed Tomography and X-ray scan, and Nuclear Magnetic Resonance are also performed to investigate the 3D expansion, nucleation and penetration, energy release, and special distribution of secondary crack development [14–17]. However, rock-like material properties are significantly influenced by ratio and curing age [18, 19]. In the current research, crack arrangements are mostly collinear or vertical noncollinear. The development of noncollinear PFN and the macromechanical behavior of PFN-containing rock mass must be further studied. The numerical simulation makes it possible to analyze the dynamic development of the secondary crack and its relationship with macroscopic stress–strain evolution of rock mass with complex PFN [20–22]. In our research, the theoretical analysis based on the sliding crack model and numerical simulation is adopted to investigate the mechanical properties of PFN-containing rock mass and the secondary crack development.

2. Secondary Crack Initiation

2.1. Sliding Crack Model. The PFN in natural rock mass can be classified into open and closed fractures. The type of fracture produced by tensile stress, which is perpendicular to the fracture surface, is called an open crack. For close fracture, the gap between fractures is filled or the surface of the fracture is shut. The secondary crack can be divided into three types, which are wing, coplanar, and out-of-plan cracks
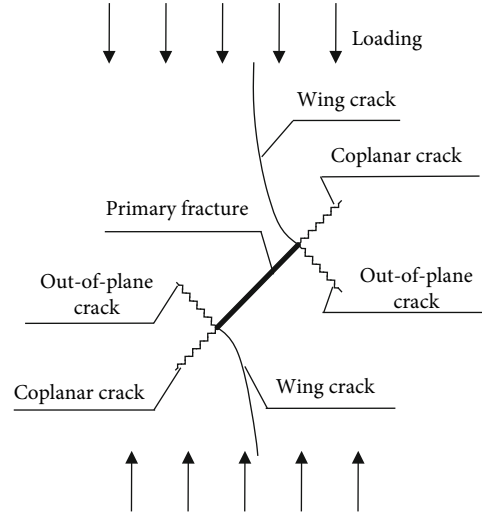
(Figure 2). The wing crack is generated by tension, and it develops along the direction of the maximum principal stress, whereas the coplanar and out-of-plan cracks are produced by shearing [23].

Basista and Gross [24] proposed the sliding crack model, which has been widely used to investigate the development mechanism of the secondary crack in brittle or quasi-brittle materials under compression [25, 26]. According to the sliding crack model (Figure 3), the components of effective shear stress τ_{eff} on the primary fracture surface are normal stress σ_n and shear stress τ. τ_{eff} can be calculated by the following equation:

$$\tau_{\text{eff}} = \tau - \mu \cdot \sigma_n, \tag{1}$$

where μ is the friction coefficient.

2.2. Closed Fracture. By applying uniformly distributed stresses σ_1 and σ_3 on the fractured rock mass, which contains a closed primary fracture, σ_n and τ on a closed fracture surface with inclination angle β can be obtained (Figure 3(a)).

$$\sigma_n = \sigma_1 + \cos^2\beta + \sigma_3 \sin^2\beta, \tag{2}$$

$$\tau = \frac{\sigma_1 - \sigma_3}{2} \sin(2\beta). \tag{3}$$

In the uniaxial compression, $\sigma_3 = 0$, Equation (2) can be simplified as follows:

$$\sigma_n = \sigma_1 \cos^2\beta, \tau = \frac{\sigma_1}{2} \sin(2\beta). \tag{4}$$

By introducing Equation (4) into Equation (1), the following equation can be obtained:

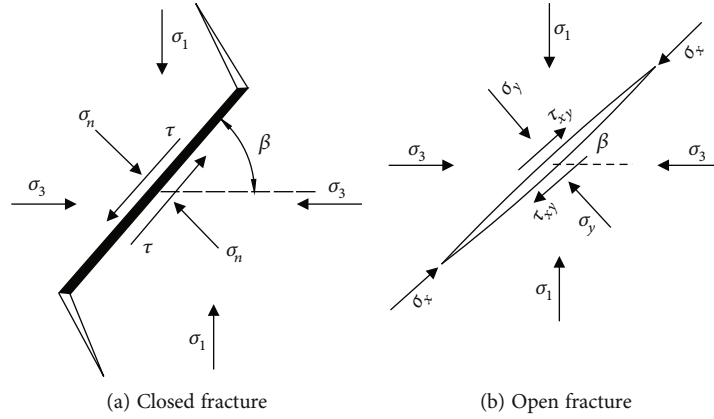$$\tau_{\text{eff}}(\beta) = \frac{\sigma_1}{2} \sin(2\beta) - \mu \cdot \sigma_1 \cos^2\beta. \tag{5}$$

(a) Closed fracture   (b) Open fracture

FIGURE 3

The PFN with different inclination angle τ_{eff} is the driving force for the relative sliding among the closed fracture surfaces and the secondary crack initiation at the tip of the fracture. Sliding crack model theory indicates that the bearing capacity of the fractured rock mass is the lowest when τ_{eff} on the crack surface is the largest. The first derivative of Equation (5) can be obtained.

$$\beta = \frac{1}{2}\operatorname{arccot}(-\mu) = \frac{1}{2}(\pi - \operatorname{arccot}\mu). \tag{6}$$

Specifically, when a closed fracture surface is closed and has no friction ($\mu = 0$), β equals 45°, whereas β is greater than 45° when $\mu \neq 0$. According to Equation (6), for the rock mass with closed PFN, the inclination angle of the fracture corresponding to the minimum strength should not be less than 45°. Moreover, β increases as the friction coefficient of the closed fracture surface increases.

2.3. Open Fracture. The open primary fracture can be equivalent to an elliptical fracture in a 2D plane [14]. Far-field stress σ_1 and σ_3 generate σ_x, σ_y, and τ_{xy} on the crack surface. σ_x and σ_y are compressive stresses in the transverse and normal direction of the primary fracture, and τ_{xy} is the shear stress. The coordinate system illustrated in Figure 3(b) can be established by taking the center of the fracture as the coordinate origin, and the vertical and parallel directions of the fracture as the vertical and horizontal axes. Based on elastic mechanic theory, σ_x, σ_y, and τ_{xy} can be calculated by the following equations:

$$\sigma_x = \sigma_1 \sin^2\beta + \sigma_3 \cos^2\beta, \tag{7}$$

$$\sigma_y = \sigma_1 \cos^2\beta + \sigma_3 \sin^2\beta, \tag{8}$$

$$\tau_{\mathrm{xy}} = \frac{\sigma_1 - \sigma_3}{2}\sin(2\beta). \tag{9}$$

Around the open crack with inclination angle β, the stress field formed by the far-field compressive stress can be regarded as the superposition of the three-component stress fields in Equation (7), which can also be transformed into the following equation under unconfined compression conditions.

$$\sigma_x = \sigma_1 \sin^2\beta,$$
$$\sigma_y = \sigma_1 \cos^2\beta, \tag{10}$$
$$\tau_{\mathrm{xy}} = \frac{\sigma_1}{2}\sin(2\beta).$$

2.4. Stress Field Influence. The analytical solution of circumferential stress around a fracture in an infinite plate under unconfined compression is shown as follows:

$$\sigma_\theta = \sigma_y \frac{1 + 2\cos 2(\theta + \beta) - 2m\cos(2\beta) - m^2}{1 - 2m\cos 2\theta + m^2}, \tag{11}$$

where $m = (a - b)/(a + b)$ and θ is the included angle of clockwise rotation with the positive direction of the x-axis as the starting position. When β equals 0°, i.e., σ_1 is perpendicular to the fracture surface, σ_θ can be calculated by the following equation:

$$\sigma_\theta = \sigma_y \frac{1 + 2\cos 2\theta - 2m - m^2}{1 - 2m\cos 2\theta + m^2}. \tag{12}$$

The extreme value of σ_θ can be obtained by taking the first derivative of Equation (12) with respect to θ and substituting the value range of m as follows:

$$(\sigma_\theta)_{\min} = \sigma_\theta|_{\theta = \pm \pi/2} = -\sigma_y. \tag{13}$$

$$(\sigma_\theta)_{\max} = \sigma_\theta|_{\theta = 0, \pi} = \sigma_y \frac{3 + m}{1 - m}. \tag{14}$$

According to Equation (13), the maximum tensile stress emerges at the end of the minor axis for the horizontal distributed elliptical fracture. When β is 90°, σ_1 is parallel to the long axis of the fracture. σ_θ can be concluded based on Equation (11) as follows:

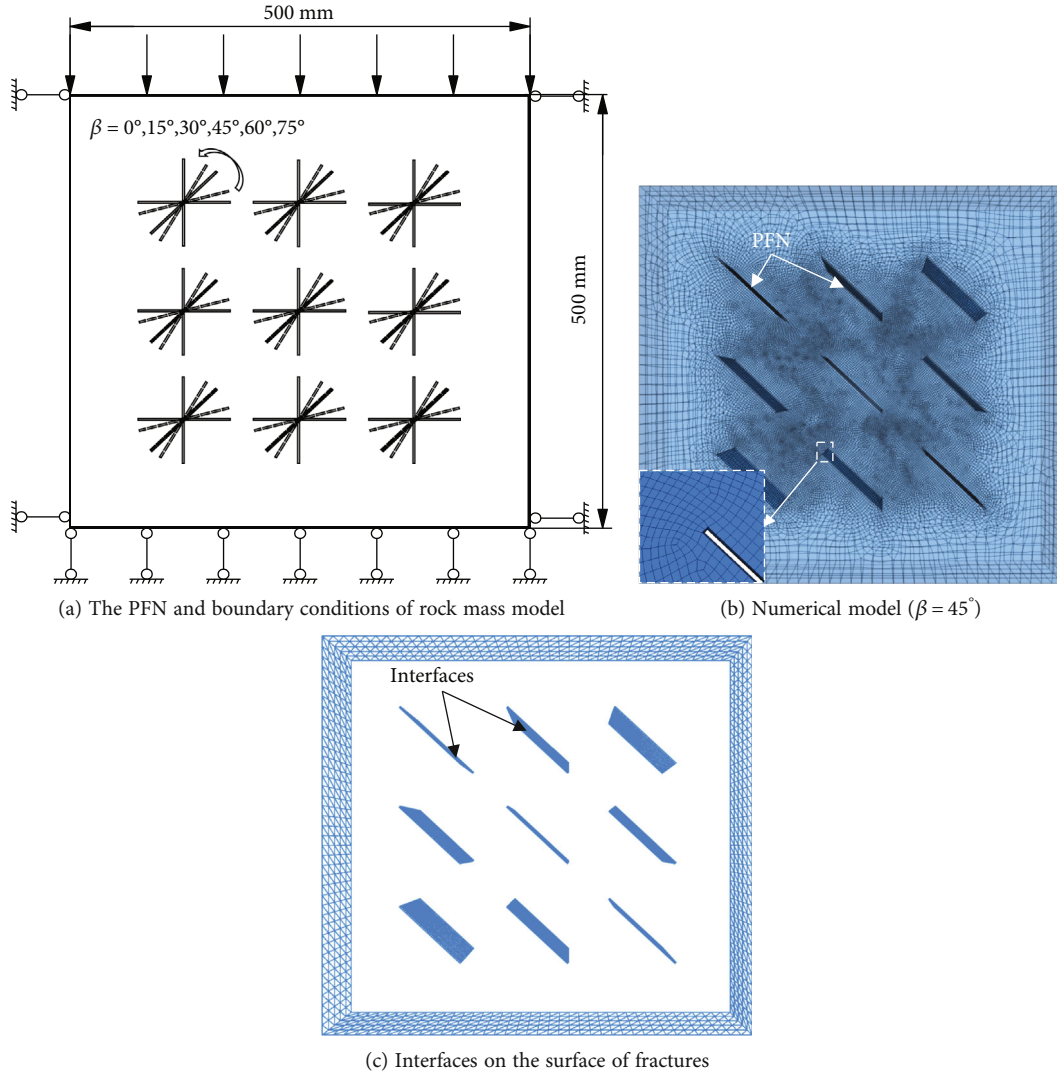$$\sigma_\theta = \sigma_x \frac{1 - 2\cos 2\theta + 2m - m^2}{1 - 2m\cos 2\theta + m^2}. \tag{15}$$

(a) The PFN and boundary conditions of rock mass model

(b) Numerical model ($\beta = 45°$)

(c) Interfaces on the surface of fractures

Figure 4: Numerical model of PFN-containing rock mass.

Therefore, the extreme values of σ_θ are presented in the following, and σ_x generates a maximum tensile stress perpendicular to σ_x near the vertex, and its value is equal to the transverse stress.

$$(\sigma_\theta)_{\min} = \sigma_\theta|_{\theta=0,\pi} = -\sigma_x,$$
$$(\sigma_\theta)_{\max} = \sigma_\theta|_{\theta=\pm\pi/2} = \sigma_x \frac{3-m}{1+m}. \tag{16}$$

Due to the low tensile strength of the rock, the shear stress on the fracture surface cannot lead to type II failure. Instead, a tensile wing crack is first formed at the tip of the primary fracture, which leads to future macroscopic failure [27]. When PFN is an open crack, the normal and lateral compressive stress forms a high-stress concentration at the boundary of PFN. For opening fractures with small β, the normal and transverse compressive stresses can still form tensile cracks even though shear stress cannot drive wing crack initiation. This is the controlling factor for the reduction of the strength of the fractured rock mass. When β
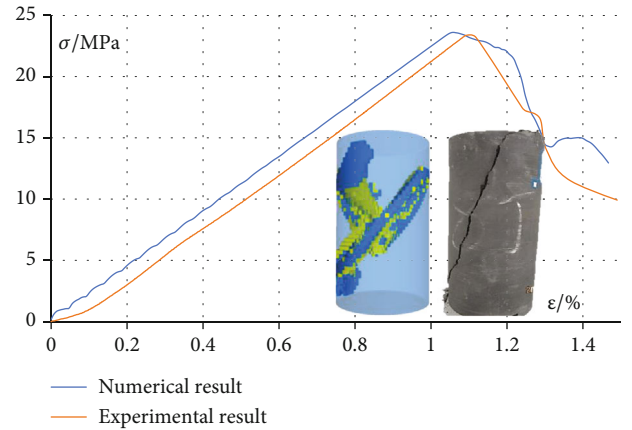

Figure 5: Parameter calibration.

increases to the point where shear stress can drive wing crack initiation, the fractured rock mass failure can be qualitatively explained by the sliding crack model. In addition, σ_x

TABLE 1: The values of parameters used in the calculation.

Elastic modular (GPa)	Poisson's ratio	Cohesion (MPa)	The angle of internal friction (°)	Strain softening				
				Plastic shear strain	0	0.02	0.05	0.07
10.5	0.21	5.7	32	Cohesion (MPa)	5.7	5.1	3.3	0.5
				The angle of internal friction (°)	32	28	15	12
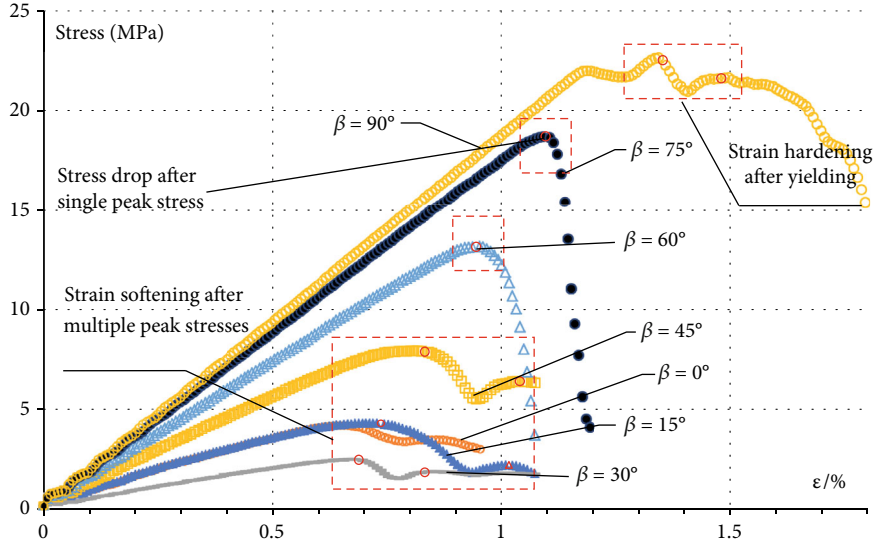
FIGURE 6: The complete stress-strain curves of PFN-containing rock mass with different β.

and σ_y affect the initiation angle and propagation path of microcracks, respectively.

3. Numerical Modeling

3.1. Model Establishment. Fast Lagrangian Analysis of Continua in 3 Dimensions (FLAC3D) is used to analyze the influence of PFN inclination on the mechanical load-bearing behavior of rock mass and the secondary crack development in this study. PFN inclination refers to the angle between the fracture and the horizontal direction. The model size is $0.5\,m \times 0.5\,m \times 0.1\,m$. The PFN introducing and meshing are completed in ANSYS. The exported nod information from ANSYS can be imported into FLAC3D and rebuild the model. The primary fractures with an opening width of 2 mm are established in the model. The inclination angle β of the PFN of each model is set to 0°, 15°, 30°, 45°, 60°, 75°, and 90° (Figure 4(a)). When $\beta = 45°$, the model is illustrated in Figure 4(b). Unconfined compression is adopted in the simulation. The displacement-controlled loading with the speed of $4 \times 10^{-5}\,mm/step$ is applied on the top boundary of the model, and the displacement constraints are imposed on other boundaries. The interfaces are added to the fracture surface to avoid zone embedding (Figure 4(c)). The mesh size of the near field of PFN is approximately 0.5 mm, which is finer than other places to restrain the calculation time and become further detailed secondary crack propagation.

3.2. Parameter Calibration. In the numerical simulation, the parameter value is essential for the calculation result. Hence, the parameter calibration must be performed first [28]. In this study, the parameter calibration target is the argillaceous sandstone selected from Chongqing, China. The stress–strain curve is obtained through the uniaxial compression test (Figure 5). UCS σ_c is 23.61 MPa, the corresponding strain ε_c for the peak stress is 1.06%, and the elastic modulus is 4.5 Gpa. The curve in the postpeak phase indicates that this kind of argillaceous sandstone is type I rock. In FLAC3D, the strain-softening model is used to describe the nonlinear mechanical behavior by degrading the cohesion and friction angle based on the plastic shear strain. Through an iterative trial-and-error process, a numerical model consistent with the mechanical properties of rock mass is obtained (Figure 5). The parameter values used in the simulation are presented in Table 1. The calibration shows that the numerical stress–strain curve and shear breakage are close to the experimental result, and the progressive failure in the postpeak phase is similar. Therefore, the parameter values can be used in the following simulation.

4. Test Results and Analysis

4.1. Stress–Strain Property. The morphology of the complete stress–strain curve also changes as PFN inclination increases (Figure 6). Morphology refers to the slope of the curve in the prepeak stage, the number of stress peaks, and the stress reduction in the postpeak phase. When β is 15°, 45°, 60°,
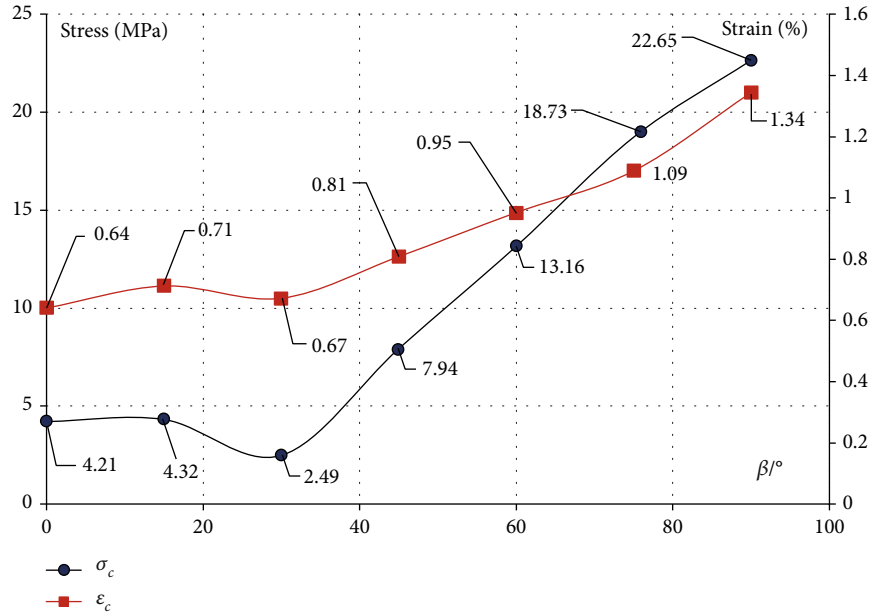
(a) σ_c and ε_c
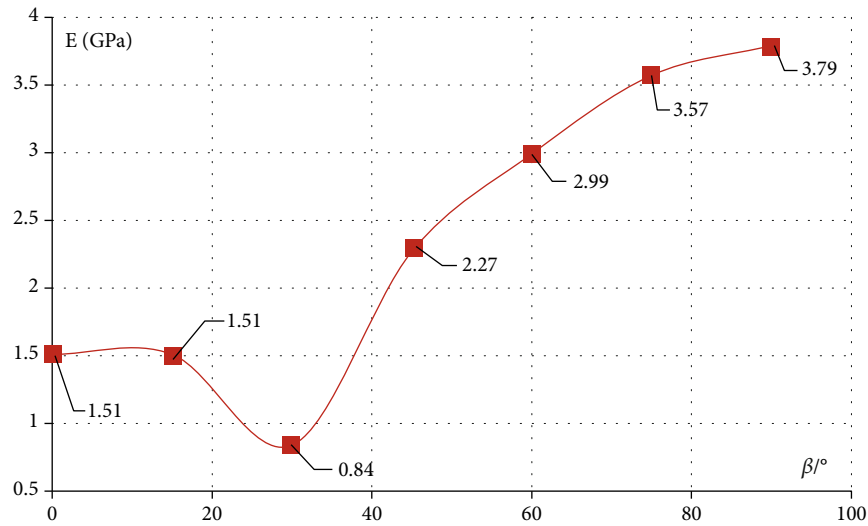
(b) Elastic modulus

FIGURE 7: The influences of β on the mechanical properties of rock mass.

and 90°, stress decreases slowly in the postpeak stage. Specifically, when $\beta = 90°$, the strain hardening behavior is more obvious after yielding. Accordingly, the model is ductile in these situations. However, when β is 60° or 75°, the model is more brittle. The stress drop rate in the postpeak stage increases significantly. This kind of breakage is close to type II rock failure. Hence, the complete stress–strain curves can be divided into two types: type I curve has multiple stress peaks and shows strain-softening characteristics in the postpeak stage when $\beta = 15°, 30°, 45°, 60°,$ and 90°. Type I curve is unimodal and with brittle failure in the postpeak stage when $\beta = 60°$ or 75°.

4.2. Strength and Elastic Modulus. Rock mass strength and deformation before failure are the important parameters

for rock breaking and supportive design in rock engineering. The effect of PFN inclination on rock mass strength and elastic modulus is shown in Figure 7(a). The ε_c and β are approximately positively correlated. However, the relationship between σ_c and β is nonlinear; when $\beta = 30°$, σ_c is the minimum value, which is 2.49 MPa; when $\beta = 0°$ and 15°, σ_c is about 4.3 MPa; when β is greater than 30°, σ_c becomes large as β increases. When $\beta = 90°$, σ_c is 22.65 MPa, and ε_c is 1.34%, which is close to the intact rock. Therefore, when the long axis of PFN is parallel to the loading direction ($\beta = 90°$), the decrease in strength is minimal, and when β is small, the influence on the stability of PFN-containing rock mass is significant. When β is 30°, it causes the greatest impact on the mechanical properties of rock mass.
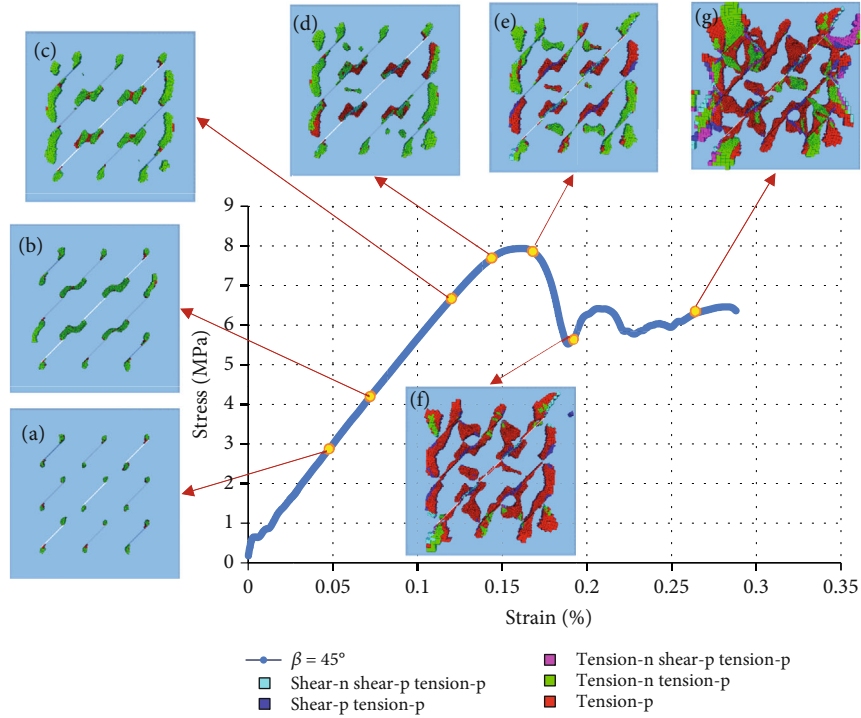
FIGURE 8: Development of secondary cracks in the rock mass with 45° PFN.

β has less effect on the elastic modulus of rock mass than that on UCS (Figure 7(b)). In general, the macroscopic elastic modulus E of rock mass decreases when β is small. When β is 0° or 15°, E is 1.51 Gpa; when β is 30°, E is the smallest, which is 0.84 Gpa. E increases as β increases. When β is 90°, E reaches the maximum value of 3.79 Gpa, which is close to the intact rock.

4.3. Secondary Crack Propagation. The propagation and penetration of secondary crack are the most essential factors affecting the load-bearing ability of rock mass. Secondary crack development in the PFN-containing rock mass and its relationship with the stress–strain curve when $\beta = 45°$ is shown in Figure 8. PFN crack initiation started in the early stage of compaction and is composed mainly of coplanar cracks (Figure 8(a)). As the load increases, coplanar cracks (generated by adjacent fractures) penetrate (Figure 8(b)) and form wing cracks along the loading direction (Figure 8(c)). Local crack propagation can lead to the insufficient fracture of the rock bridge, but the rock mass failure does not occur. In the aforementioned stages, the secondary crack is mainly a tensile crack. The rock mass loses its bearing capacity when the primary fracture and the secondary crack form the dominant fracture surface in it. The primary fracture does not completely cut the rock bridge along the main shear direction. The bearing capacity of model is not completely lost. The stress rises in postpeak stage as can be seen from Figure 8(f). In addition, due to the frictional slippage of the broken rock on the fracture surface, the rock still has residual strength in the postpeak stage (Figure 8(g)).

The plastic zone development inside the PFN-containing rock mass at different strains is illustrated in Figure 9. Rock mass failure with different PFN inclination angles has some common characteristics. Under compaction, the nonuniform distribution of internal stress leads to preferential cracking at the ends and in the middle of fractures. Secondary crack growth is relatively independent of each other in the early stage of compaction within a limited time and space around the fracture (Figures 9(a), 9(q), and 9(u)). The newly generated plastic zone is mainly tension failure or tension-shear mixed failure within this stage. Rock block movement is dominated by frictional slippage along the fracture surface after the visible model damage (Figures 9(f)– 9(h)). Therefore, the tensile failure of a plastic zone gradually transforms into shear failure in the postpeak stage (Figures 9(c), 9(g), 9(k), 9(o), 9(s), and 9(v)).

According to the location and growth of PFN, the secondary crack can be divided into the following four types: type I is the coplanar crack that emerges in the rock bridge along the long axis direction of the primary fracture. Type II is the boundary wing crack, which is arc-shaped and formed around PFN. Its development direction is similar to the loading direction. Type III is the near-field wing crack that is approximately in the plane direction of PFN. The development direction of type III crack is nearly perpendicular to the normal direction of PFN. Type IV is the macroscopic shear crack that is formed by the convergence of secondary shear cracks in a certain direction.

4.4. β Effect. Secondary crack development in PFN-containing rock mass has some particularities as β changes.

(1) When β is 0°, the first damaged area is located in the middle of the fracture, mainly tensile failure. The

(1) $\beta = 0°$

(2) $\beta = 15°$

(3) $\beta = 30°$

(4) $\beta = 45°$

(5) $\beta = 60°$

(6) $\beta = 75°$

Shear-n shear-p
Shear-n shear-p tension-p
Shear-n tension-p
Shear-p

Shear-p tension-p
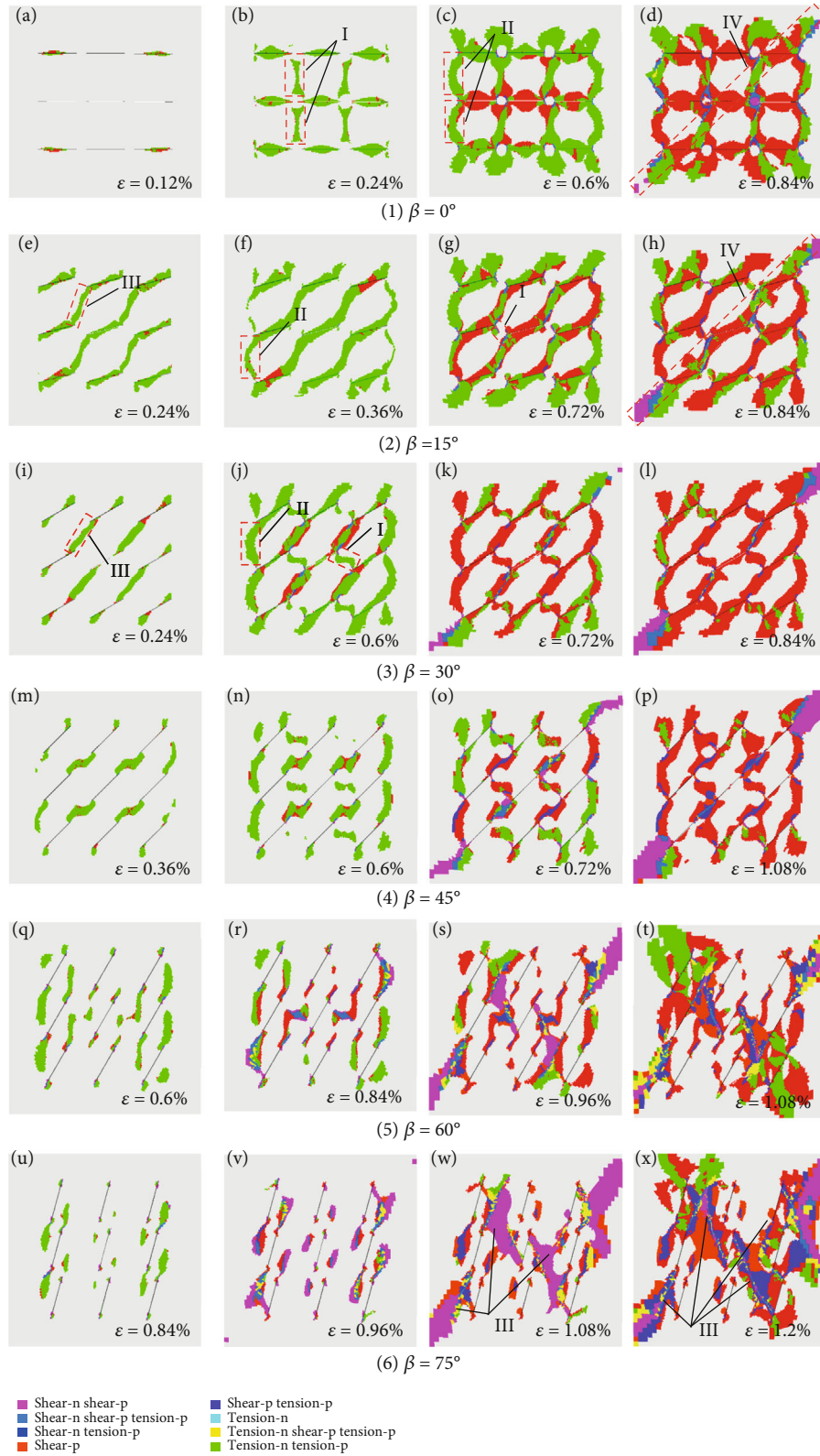Tension-n
Tension-n shear-p tension-p
Tension-n tension-p

FIGURE 9: Failure of jointed rock mass.

vertical tensile crack in the middle of a horizontal open fracture develops preferentially (Figure 9(a)), which is consistent with the result of Equation (13). Type I crack expands and connects the upper and lower fractures in the vertical direction in the early stage with the increasing load and then type II crack emerges (Figures 9(b) and 9(c)). Type IV single shear crack, which is oblique to
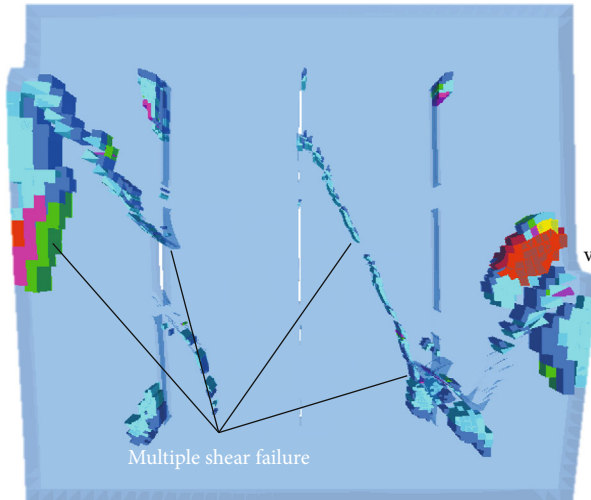
FIGURE 10: Failure of the model when $\beta = 90°$.

the loading direction, is formed and leads to rock mass failure

(2) When β is between 15° and 45°, type III crack is initiated preferentially and connects adjacent fractures (Figures 9(e), 9(i), and 9(m)). Subsequently, types I and II begin to show up as compaction rises. Type IV crack is mainly developed from the further growth of type III crack (Figures 10(h), 10(l), and 10(p)). Types I and II develop almost simultaneously when $\beta = 15°$ and 30° (Figures 9(f) and 9(j)). Type II crack is formed and developed earlier than type I fractures when β is 45° (Figures 9(m) and 9(n))

(3) When β is 60° or 75°, secondary crack initiation starts at $\varepsilon = 0.5\%$, which is slower than in other situations, and crack location is irregular (Figures 10(q) and 10(u)). The macroscopic model failure is no longer dominated by type III crack but transforms into multiple shear failures (Figures 10(s), 10(t), 10(w), and 10(x)). PFN development when β is 60° or 75° has a smaller influence on the failure characteristics and mechanical properties of rock mass than it is when β is between 15° and 45°. The UCS and elastic modulus of rock mass are also close to the complete rock

(4) When β is 90°, the progressive development of the plastic zone is not obvious, but type IV crack rapidly grows within 0.5% of strain. Rock mass failure is dominated by multiple shears and tensile failures (Figure 10). Little interconnection exists between the dominant crack and PFN. PFN also has less effect on the deterioration of the mechanical properties of the model

(5) PFN inclination has the greatest influence on the mechanical behavior of rock mass when β is 30°. According to the crack initiation mechanism of the open fracture, the effective shear force on the crack

surface is 0 when β is 90°. No driving force is observed at the tip of the fracture to produce micro secondary crack, and normal stress σ_n is vertical to the closed crack surface. It also contributes little to the stress concentration at the tip of the fracture. σ_n is the same when σ_n is 0° and 90°. However, the new tensile–shear stress formed at the tip of the open crack lowers the threshold for crack propagation and causes the deterioration of the macroscopic mechanical properties of rock mass

(6) According to Figure 6, for type I curve, the reason for the single stress peak and the rapid decrease of stress after failure is that PFN propagation in rock mass forms a dominant fracture, which is before the fracture propagation in other zones. After the failure of the core bearing part of the rock mass, the stress drop occurs rapidly. Subsequently, the rock mass in the noncore load-bearing area continues to be loaded and damaged, and the broken rock blocks slide along fracture surfaces, making the full stress–strain curve a type II curve

5. Conclusion

The mechanical behavior of rock mass with a different PFN inclination is investigated in this research. Through the numerical simulation of unconfined compression, the bearing capacity, failure mode, and secondary crack propagation are analyzed. The main conclusions are as follows:

(1) The inclination angle of PFN has a significant nonlinear influence on the mechanical behavior of rock mass. The strength and elastic modulus decrease when the inclination angle is between 0° and 45°. The impact of PFN reaches its maximum when β is 30°, and the mechanical properties of rock mass are close to the intact rock when β is 90°

(2) The stress–strain curves of PFN-containing rock mass can be divided into two types: type I curve is with multipeak and strain softening in the postpeak stage when β is 15°, 30°, 45°, 60°, and 90°; type II curve is unimodal and with brittle failure when β is 60° and 75°

Secondary crack propagation can be classified into four main types: type I is the coplanar crack, type II is the wing crack around PFN, type III is the near-field wing crack, and type IV is the macroscopic shear crack.

(3) Due to continuously increased loading, the tip of the fracture cracks first, and the main damage is the tension and shear mixed. Secondary crack propagation can be divided into four types: type I is the coplanar crack, type II is the wing crack around PFN, type III is the near-field wing crack, and type IV is the macroscopic shear crack. Type IV crack is mainly developed from type III crack when β is between 0° and 45°. Rock mass failure involves multiple shears, and

the influence of PFN and secondary crack propagation on the degeneration of mechanical properties of rock mass is weakened when β is larger than 60°

Data Availability

The data are available on request due to privacy/ethical restrictions.

Conflicts of Interest

The authors declare that they have no known competing financial interests or personal relationships that could influence the work presented in this paper.

Funding

References

[1] H. Rehman, W. Ali, A. M. Naji, J. J. Kim, R. A. Abdullah, and H. K. Yoo, "Review of rock-mass rating and tunneling quality index systems for tunnel design: development, refinement, application and limitation," *Applied Sciences*, vol. 8, no. 8, p. 1250, 2018.

[2] E. Hoek and M. S. Diederichs, "Empirical estimation of rock mass modulus," *International Journal of Rock Mechanics and Mining Sciences*, vol. 43, no. 2, pp. 03–215, 2006.

[3] E. Mutaz, M. Serati, and D. J. Williams, "Crack initiation evolution under triaxial loading conditions," *IOP Conference Series: Earth and Environmental Science*, vol. 833, no. 1, article 012012, 2021.

[4] G. R. Irwin, "Analysis of stresses and strains near the end of a crack traversing a plate," *Journal of Applied Mechanics*, vol. 24, no. 3, pp. 361–364, 1957, Trans. ASME, Ser. E,.

[5] E. Hoek and Z. T. Bieniawski, "Brittle fracture propagation in rock under compression," *International Journal of Fracture Mechanics*, vol. 1, no. 3, pp. 137–155, 1965.

[6] S. Peng and A. M. Johnson, "Crack growth and faulting in cylindrical specimens of Chelmsford granite," *International Journal of Rock Mechanics and Mining Sciences & Geomechanics Abstracts*, vol. 9, no. 1, pp. 37–86, 1972.

[7] R. H. Wong and K. T. Chau, "Crack coalescence in a rock-like material containing two cracks," *International Journal of Rock Mechanics and Mining Sciences*, vol. 35, no. 2, pp. 147–164, 1998.

[8] E. Hosseinian, S. Gupta, O. N. Pierron, and M. Legros, "Size effects on intergranular crack growth mechanisms in ultrathin nanocrystalline gold free-standing films," *Acta Materialia*, vol. 143, pp. 77–87, 2018.

[9] Z. Aliabadian, M. Sharafisafa, F. Tahmasebinia, and L. Shen, "Experimental and numerical investigations on crack development in 3D printed rock-like specimens with pre-existing flaws," *Engineering Fracture Mechanics*, vol. 241, article 107396, 2021.

[10] M. R. Vergara, M. V. S. Jan, and L. Lorig, "Numerical model for the study of the strength and failure modes of rock containing non-persistent joints," *Rock Mechanics and Rock Engineering*, vol. 49, no. 4, pp. 1211–1226, 2016.

[11] Y. Wang, J. Han, Y. Xia, and D. Long, "New insights into the fracture evolution and instability warning predication for fissure-contained hollow-cylinder granite with different hole diameter under multi-stage cyclic loads," *Theoretical and Applied Fracture Mechanics*, vol. 119, article 103363, 2022.

[12] A. Kumar and G. U. Kulkarni, "Time evolution and spatial hierarchy of crack patterns," *Langmuir*, vol. 37, no. 44, pp. 13141–13147, 2021.

[13] A. Spetz, R. Denzer, E. Tudisco, and O. Dahlblom, "Phase-field fracture modelling of crack nucleation and propagation in porous rock," *International Journal of Fracture*, vol. 224, no. 1, pp. 31–46, 2020.

[14] X. Lei, K. Masuda, O. Nishizawa et al., "Detailed analysis of acoustic emission activity during catastrophic fracture of faults in rock," *Journal of Structural Geology*, vol. 26, no. 2, pp. 247–258, 2004.

[15] Y. Wang, Y. Su, Y. Xia, H. Wang, and X. Yi, "On the effect of confining pressure on fatigue failure of block-in-matrix soils exposed to multistage cyclic triaxial loads," *Fatigue & Fracture of Engineering Materials & Structures*, vol. 45, no. 9, pp. 2481–2498, 2022.

[16] Y. Wang, T. Mao, Y. Xia, X. Li, and X. Yi, "Macro-meso fatigue failure of bimrocks with various block content subjected to multistage fatigue triaxial loads," *International Journal of Fatigue*, vol. 163, no. article 107014, 2022.

[17] D. Li, E. Wang, X. Kong, M. Ali, and D. Wang, "Mechanical behaviors and acoustic emission fractal characteristics of coal specimens with a pre-existing flaw of various inclinations under uniaxial compression," *International Journal of Rock Mechanics and Mining Sciences*, vol. 116, pp. 38–51, 2019.

[18] M. Sharafisafa, L. Shen, Y. Zheng, and J. Xiao, "The effect of flaw filling material on the compressive behaviour of 3D printed rock-like discs," *International Journal of Rock Mechanics and Mining Sciences*, vol. 117, pp. 105–117, 2019.

[19] Z. Aliabadian, G. Zhao, and A. R. Russell, "Failure, crack initiation and the tensile strength of transversely isotropic rock using the Brazilian test," *International Journal of Rock Mechanics and Mining Sciences*, vol. 122, article 104073, 2019.

[20] M. Laghaei, A. Baghbanan, H. Hashemolhosseini, and M. Dehghanipoodeh, "Numerical determination of deformability and strength of 3D fractured rock mass," *International Journal of Rock Mechanics and Mining Sciences*, vol. 110, pp. 246–256, 2018.

[21] Y. Wang, X. Yi, P. Li, M. Cai, and T. Sun, "Macro-meso damage cracking and volumetric dilatancy of fault block-in-matrix rocks induced by freeze–thaw-multistage constant amplitude cyclic (F-T-MSCAC) loads," *Fatigue & Fracture of Engineering Materials & Structures*, vol. 45, no. 10, pp. 2990–3008, 2022.

[22] J. Singh, S. P. Pradhan, M. Singh, and B. Yuan, "Modified block shape characterization method for classification of fractured rock: a python-based GUI tool," *Computers & Geosciences*, vol. 164, article 105125, 2022.

[23] H. Haeri, K. Shahriar, M. F. Marji, and P. Moarefvand, "Experimental and numerical study of crack propagation and coalescence in pre- cracked rock-like disks," *International Journal of Rock Mechanics and Mining Sciences*, vol. 67, pp. 20–28, 2014.

[24] M. Basista and D. Gross, "The sliding crack model of brittle deformation: an internal variable approach," *International Journal of Solids and Structures*, vol. 35, no. 5-6, pp. 487–509, 1998.

[25] Y. Li and C. Yang, "On sliding crack model for brittle solids," *International Journal of Fracture*, vol. 142, no. 3-4, pp. 323–330, 2007.

[26] B. Paliwal and K. T. Ramesh, "An interacting micro-crack damage model for failure of brittle materials under compression," *Journal of the Mechanics and Physics of Solids*, vol. 56, no. 3, pp. 896–923, 2008.

[27] C. Zhu, Z. Yin, and C. Li, "Crack initiation extension law of opening type crack under compression state," *Journal of Liaoning Technical University (Natural Science)*, vol. 35, no. 10, pp. 1105–1110, 2016.

[28] G. Li, S. Cao, and H. Yang, "Study on bearing and failure laws of roadside support influenced by end restraint," *Journal of Mining & Safety Engineering*, vol. 33, no. 4, pp. 706–712, 2016.